Nuclear Instruments and Methods in Physics Research A 797 (2015) 290–296

Contents lists available at ScienceDirect

Nuclear Instruments and Methods in Physics Research A

journal homepage: www.elsevier.com/locate/nima

Spectrum correction algorithm for detectors in airborne radioactivity monitoring equipment NH-UAV based on a ratio processing method

Ye Cao [a], Xiao-Bin Tang [a,b,*], Peng Wang [a], Jia Meng [a], Xi Huang [a], Liang-Sheng Wen [a], Da Chen [a,b]

[a] Department of Nuclear Science and Engineering, Nanjing University of Aeronautics and Astronautics, Nanjing 210016, China
[b] Jiangsu Key Laboratory of Nuclear Energy Equipment Materials Engineering, Nanjing University of Aeronautics and Astronautics, Nanjing 210016, China

ARTICLE INFO

Article history:
Received 20 March 2015
Received in revised form
10 June 2015
Accepted 10 July 2015
Available online 16 July 2015

Keywords:
Nuclear accident
Detector
Monte Carlo
Gamma-spectrum correction

ABSTRACT

The unmanned aerial vehicle (UAV) radiation monitoring method plays an important role in nuclear accidents emergency. In this research, a spectrum correction algorithm about the UAV airborne radioactivity monitoring equipment NH-UAV was studied to measure the radioactive nuclides within a small area in real time and in a fixed place. The simulation spectra of the high-purity germanium (HPGe) detector and the lanthanum bromide ($LaBr_3$) detector in the equipment were obtained using the Monte Carlo technique. Spectrum correction coefficients were calculated after performing ratio processing techniques about the net peak areas between the double detectors on the detection spectrum of the $LaBr_3$ detector according to the accuracy of the detection spectrum of the HPGe detector. The relationship between the spectrum correction coefficient and the size of the source term was also investigated. A good linear relation exists between the spectrum correction coefficient and the corresponding energy ($R^2=0.9765$). The maximum relative deviation from the real condition reduced from 1.65 to 0.035. The spectrum correction method was verified as feasible.

© 2015 Elsevier B.V. All rights reserved.

1. Introduction

At present, nuclear power is undergoing rapid development worldwide. As the lifeline of nuclear power, nuclear security is at the foundation of the development of nuclear power. When a nuclear accident happens, radioactive substances, which can cause significant harm, are released into the environment. Therefore, information on the distribution of nuclides in the environment after a nuclear accident should be rapidly and accurately obtained. Among the existing methods used in the event of a nuclear accident, detecting and measuring radioactive nuclides in the environment using an unmanned aerial vehicle (UAV) is reliable and efficient. Canada, Finland and Israel developed radioactivity monitoring equipment installed on UAVs [1–12]. However, these devices significantly differ in radiation detection accuracy; thus, further research is necessary.

For our research project, we developed a UAV airborne radioactivity monitoring equipment called "NH-UAV" (Fig. 1). The purpose of this equipment is to measure radioactive nuclides in real time and in a fixed place after a nuclear accident. We selected a double detector system that contains a high-purity germanium (HPGe) semiconductor detector and a lanthanum bromide ($LaBr_3$) scintillator detector. As shown in Fig. 1, B denotes the $LaBr_3$ scintillator detector whose probe is directly exposed to air. The $LaBr_3$ detector can detect a certain range of radioactivity including all radioactive aerosols in the air and radioactive gases. C presents the HPGe detector. The probe of this detector has a filter at the front, and the sample in the filter is checked every 10 min. The HPGe detector can only detect radioactive aerosols absorbed by the filter because of shielding in the device. The main purpose of the double detectors was to enable each detector to back up, supply and verify the detection data of the other. Such data included radionuclides in radioactive aerosols and radioactive gases within a certain space. Radioactive aerosols can be absorbed by the filter and detected precisely by the HPGe detector. However, the HPGe detector cannot detect radioactive gases because of shielding in the device. Meanwhile, the $LaBr_3$ detector placed in open space can detect radioactive aerosols and radioactive gases within a certain space; however, its detection data are affected by radioactivity in the distance. Therefore, we cannot directly obtain precise information on radioactivity within a small area.

To obtain precise information on the detected radioactivity within a small area, the detection data of the HPGe detector and

* Corresponding author at: Department of Nuclear Science and Engineering, Nanjing University of Aeronautics and Astronautics, Nanjing 210016, China.
Tel.: +86 13601582233; fax: +86 25 52112906x80407.
E-mail address: tangxiaobin@nuaa.edu.cn (X.-B. Tang).

http://dx.doi.org/10.1016/j.nima.2015.07.012
0168-9002/© 2015 Elsevier B.V. All rights reserved.

the $LaBr_3$ detector should be corrected. That is, the precise types and activities of radioactive nuclides within a small scope can be obtained using a certain algorithm to validate, supply, and optimize detection data. Therefore, the current study mainly examined the correction algorithm of the detection spectrum generated by the NH-UAV.

2. Materials and methods

2.1. Monte Carlo simulation

In this research, the simulations of the two detectors were performed using a MC N-particle transport code system (MCNP) [13]. MCNP is a large multifunctional calculation program compiled by the Monte Carlo Team of the Los Alamos National Laboratory in the United States. The HPGe detector used in this research was Trans-SPEC-100 T manufactured by ORTEC. The detector's crystal dimensions given by the manufacturer are: 6.7 cm diameter, 5.2 cm high and 1 cm from the top of the detector's crystal to the entrance window. Meanwhile, the $LaBr_3$ detector was procured from Saint-Gobain S.A., and a 1.5 in. × 1.5 in. cylindrical crystal was used here. The calculation models of the two detectors are shown in Fig. 2.

During MCNP simulation, the integrated current over a surface is obtained using the F1 tally. Meanwhile, the F8 tally provides the energy distribution of pulses created in a detector by radiation and is called a pulse height tally [13]. In this paper, the spectrum generated by the HPGe detector could be obtained directly by using the F8 tally. However, for the $LaBr_3$ detector, the error in the simulation results was significant if the spectrum was directly calculated using the F8 tally. Because the sizes of the source term considered in this paper were relatively large. Thus, the secondary source method was used to reduce the variance. The detailed approach of the secondary source method (Fig. 3) is described as follows. In general, the secondary method included four steps. Firstly, a sphere with a radius of 1 m was set around the detector. Gamma rays emitted from radioactive materials inside the spherical shell (ranging from 1 m to 1000 m) could be recorded as the integrated current over the sphere surface with a radius of 1 m using the F1 tally. Since the difference between the source particles is very small, we can suppose the source term of the spherical shell from 1 m to 1000 m is isotropic and uniform. Secondly, the gamma particles flux incident to the sphere surface with a radius of 1 m was used as the secondary source to obtain the pulse amplitude spectrum of the sphere source using the F8 tally. In other words, the particles flux obtained according to the F1 tally were equivalent to the particles flux of the spherical shell from 1 m to 1000 m. The source term here was set to a cosine distribution. Thirdly, the gamma rays emitted from radioactive materials inside the sphere with a radius of 1 m were recorded using the F8 tally to obtain the pulse amplitude spectrum. The source distribution was set to an isotropic and uniform sphere source distribution. Finally, the data of spectrum were the sum between the detection counts of the sphere surface with the radius of 1 m and the detection counts of the sphere with a radius of 1 m, and the data of two parts were obtained using the F8 tally based on the $LaBr_3$ detector. In the processing of simulation, the NPS of each program was set to 2×10^{10}.

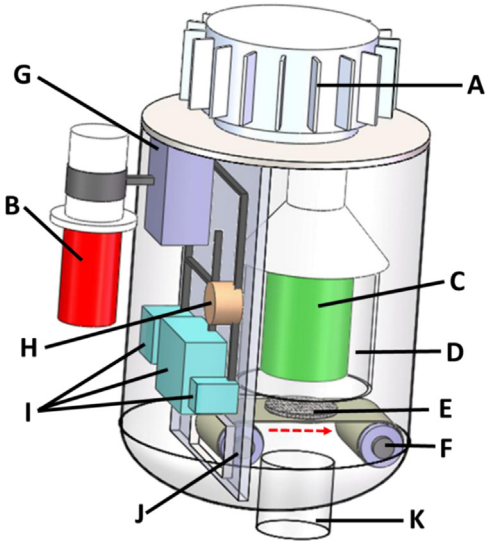

Fig. 1. Schematic diagram of the NH-UAV: A – data acquisition unit, B – $LaBr_3$ scintillator detector, C – HPGe semiconductor detector, D – shield, E – radionuclide acquisition unit, F – roller, G – power supply unit, H – GM-counter, I – electronics unit, J – support structure, and K – air inlet.

2.2. Source term

The categories and activities of the radioactive nuclides could be obtained from Ref. [14], which was published after the Fukushima nuclear accident. The radioactivity considered was within 20 km around the nuclear plant. Table 1 shows the main radioactive nuclides and their respective activities. The HPGe detector was mainly used to detect the radioactive aerosols absorbed by the filter whose filtering efficiency and filtering time were 30% and 10 s respectively. Meanwhile, the energies used in this study were ranging from 80 keV to 1800 keV considering numbers of the gamma rays emitted from radioactive materials. The spectrum correction method proposed thereinafter was mainly used to correct radioactive gases in nuclear accidents. Radioactive gases refer to ^{133}Xe and ^{88}Kr whose energies of gamma rays are higher than 80 keV. On the other hand, the

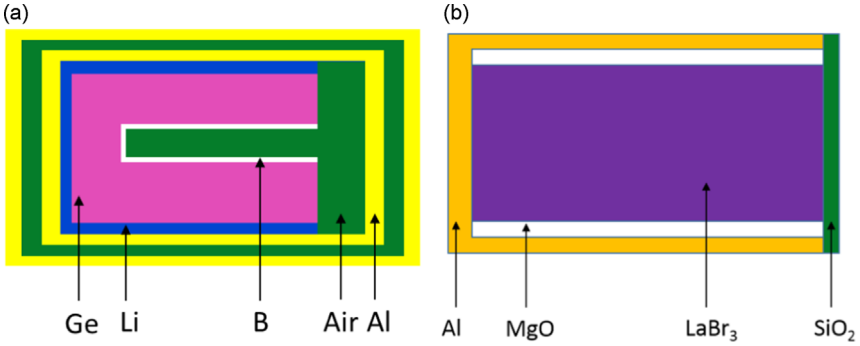

Fig. 2. Calculation models of the two detectors (a) HPGe detector and (b) $LaBr_3$ detector.

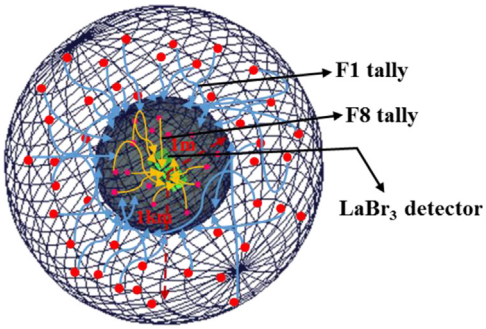

Fig. 3. Schematic of the secondary source method.

Table 1
Main radioactive nuclides and activities after the Fukushima nuclear accident.

Radioactive nuclide	Activity (Bq)	Radioactive nuclide	Activity (Bq)	Radioactive nuclide	Activity (Bq)
^{133}Xe	1.1×10^{19}	^{127m}Te	1.1×10^{15}	^{131}I	1.6×10^{17}
^{134}Cs	1.8×10^{16}	^{129m}Te	3.3×10^{15}	^{133}I	6.8×10^{14}
^{137}Cs	1.5×10^{16}	^{131m}Te	9.7×10^{13}	^{135}I	6.3×10^{14}
^{89}Sr	2.0×10^{15}	^{132}Te	7.6×10^{14}	^{127}Sb	6.4×10^{15}
^{140}Ba	3.2×10^{15}	^{239}Np	7.6×10^{13}	^{129}Sb	1.6×10^{14}

radioactive nuclides released in nuclear accidents are basically the same. So the energy scope selected here is reasonable.

To simulate actual air radiation monitoring conditions accurately, a sphere volumetric source was used to simulate the radioactive plume. The required radius R, which was covered by gamma-rays in the air to reduce the density I to 0.3% of its initial value I_0, mainly depended on the energy [15]. The 0.3% was selected arbitrarily here.

On one hand

$$I = I_0 e^{-\mu(E)R} \tag{1}$$

where I_0 and I represent the intensity of the γ-rays before and after passing through the material respectively; $\mu(E)$ is the linear attenuation coefficient in the material; and R is the thickness of the material. On the other hand

$$I = 0.003 I_0 \tag{2}$$

According to Eqs. (1) and (2)

$$R_m = \frac{5.809143}{\mu(E)} \tag{3}$$

In the present study, the highest energy of the γ-rays in the source term was 1.791 MeV and its linear attenuation coefficient in the air was 6.14361×10^{-3} m^{-1}. Thus the required radius R was calculated as follows:

$$R_m = \frac{5.809143}{\mu(E)} = \frac{5.809143}{4.75144\times10^{-3}\ \mathrm{m^2/kg}\times 1.293\ \mathrm{kg/m^3}} = 945.559\ \mathrm{m} \tag{4}$$

Therefore we could set the radius of the sphere volumetric source to 1 km to simulate the detection zone of the $LaBr_3$ detector.

2.3. Efficiency calibration

Detection efficiencies are mainly categorized into source peak efficiency which is also called the absolute calibration and intrinsic peak efficiency based on the nature of the recorded event. Source peak efficiency is defined as follows:

$$\varepsilon_{sp} = \frac{\text{number of photons detected under full-energy peak}}{\text{number of photons emitted by source}} \tag{5}$$

It is dependent on both detector properties and on the details of the counting geometry (primarily the distance from the source to the detector). Intrinsic peak efficiency is defined as follows:

$$\varepsilon_{ip} = \frac{\text{number of photons detected under full-energy peak}}{\text{number of photons incident on detector}} \tag{6}$$

It typically depends primarily on the detector material, the energy of the γ-ray, and the physical thickness of the detector in the direction of the incident gamma rays [16–20]. During the calculation of efficiency, the net full-energy peak area is obtained using the total peak area method [21,22]. Its computational formula is as follow:

$$S = \sum_{i=l}^{h} y_i - \frac{h-l+1}{2}(y_l + y_h) \tag{7}$$

where S is the net full-energy peak area; l and h represent the boundary channels on both sides of full-energy peak respectively; the y_l and y_h are the numbers of the channel l and the channel h respectively; and y_i denotes the number of counts in the considered channel.

Considering the difference between the detection zones of the HPGe detector and the $LaBr_3$ detector, the efficiency calibration in the two detectors would be different. The HPGe detector could detect information on radioactive aerosols within a small area; thus, we could obtain activity information on radioactive aerosols within a small area after source peak efficiency calibration. The radioactive nuclides from the distance would contribute to the spectrum of the $LaBr_3$ detector. Activity information on radioactive aerosols and radioactive gases around the detector could be obtained after intrinsic peak efficiency calibration. Consequently, the HPGe detector would be calibrated by the source peak efficiency, whereas the $LaBr_3$ detector would be calibrated by the intrinsic peak efficiency.

3. Results and discussion

3.1. MC simulation

The simulation gamma-ray spectra of the double detectors could be obtained by simulating the detection zones of the HPGe detector and the $LaBr_3$ detector after the Fukushima nuclear accident.

Some experiments about the energy resolutions of the double detectors also were conducted using the radionuclide ^{60}Co before the MCNP simulations were performed. The energy resolutions of the HPGe detector and the $LaBr_3$ detector were 0.76% and 2.92% at 1173 keV respectively. They were 0.77% and 2.95% at 1332 keV. Meanwhile, experiments on detection capability of the $LaBr_3$ detector in low energies (below 100 keV) were also performed using radionuclides ^{238}Pu and ^{241}Am. The $LaBr_3$ detector can detect the particles in low energies (below 100 keV) according to the experimental energy spectrum. What is more, there only was 80 keV about the energy of gamma-ray in low energy and its concentration was big relative to other energies in the study.

The MC simulation spectra of the HPGe detector and the $LaBr_3$ detector are shown in Fig. 4. According to the results of experiments and simulations, the energy resolution of the HPGe detector is distinctly superior to that of the $LaBr_3$ detector. The obtained counts in the $LaBr_3$ detection spectrum were higher than those in

the HPGe detection spectrum. The spectrum of the $LaBr_3$ detector included information on the radioactive gas ^{133}Xe and on the radioactive aerosols ^{131}I and ^{137}Cs among others. However, the spectrum of the HPGe detector only included information on the radioactive aerosols ^{131}I and ^{137}Cs among others, and did not include information on the radioactive gas ^{133}Xe.

3.2. Efficiency calibration

The detection spectrum of the HPGe detector could be obtained by simulating a series of nuclides based on MCNP. Then, the source peak efficiency of the HPGe detector was calculated according to Eq. (5). The source peak efficiency of the HPGe detector and its fitting curve are shown in Fig. 5.

Similarly, the spectrum of the gamma-ray was calculated using MC software. The numbers of particles in the sensitive volume of the $LaBr_3$ detector were obtained based on the F1 tally. In the course of the intrinsic peak efficiency calibration about the $LaBr_3$ detector, a sphere source was set for the source term in this study. The source particles were generated uniformly on the surface of the crystal. Then, the intrinsic peak efficiency was calculated according to Eq. (6). The intrinsic peak efficiency of the $LaBr_3$ detector and its fitting curve are shown in Fig. 6.

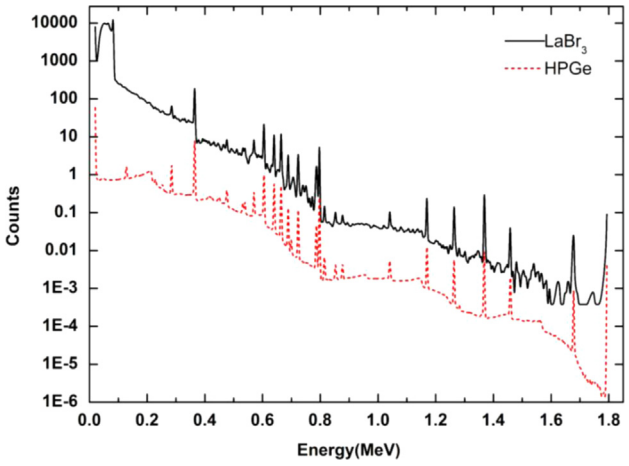

Fig. 4. Simulation gamma-ray spectra of the two detectors. The black solid curve denotes the spectrum of the $LaBr_3$ detector and the red dash curve refers to the spectrum of the HPGe detector.

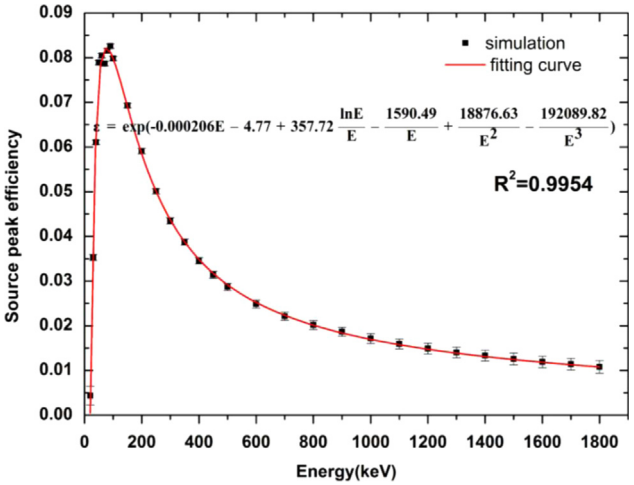

Fig. 5. Source peak efficiency calibration fitting curve of the HPGe detector.

3.3. Spectrum correction method

The spectrum correction method proposed in this study was based on the detection differences between the double detectors in the equipment NH-UAV. That is to say, the HPGe detector could detect radioactive aerosols absorbed in the filter within the volume of 1 m^3, while the $LaBr_3$ detector could detect radioactive aerosols and radioactive gases. Meanwhile, the gamma rays in the distance would make contributions to the spectra of the $LaBr_3$ detector. The ratio values relative to 364.5 keV were accurate in the spectra of the HPGe detector. Thus, the spectra of the HPGe detector were used as standard spectra to correct the spectra of the $LaBr_3$ detector. Specifically, the spectrum correction method was performed using the relative proportion in the net full-energy peak area in the same spectrum. The net full-energy peak area was calculated using Eq. (7). After the corresponding efficiency was calibrated, the full-energy peak area could be obtained. In the same spectrum, using the full-energy peak area with energy of 364.5 keV to be a benchmark, the relative proportion of other energies to 364.5 keV could be obtained in the detection spectra of the HPGe detector and the $LaBr_3$ detector.

Considering the full-energy peak area with energy of 364.5 keV in the detection spectra of the HPGe detector and the $LaBr_3$ detector as benchmarks, the net peak areas after the calibration of 364.5 keV were set to A_0 and B_0 respectively. The corresponding peak areas of other energies were set to A_i and B_i. Then, the relative proportion in two spectra could be calculated as follows.

The ratio relative to 364.5 keV in the spectrum of the HPGe detector (the ideal relative) is

$$R_{Ai} = A_i / A_0 \tag{8}$$

The ratio relative to 364.5 keV in the spectrum of the $LaBr_3$ detector (the real relative) is

$$R_{Bi} = B_i / B_0 \tag{9}$$

Finally, the spectrum correction coefficients were calculated according to the ratio between the real relative and the ideal relative as follows:

$$R_i = R_{Bi} / R_{Ai} \tag{10}$$

Table 2 shows the corresponding data of all energies obtained by conducting relative data treatment according to Eqs. (8)–(10). The spectrum correction coefficients were calculated using Eq. (10).

The numbers of Table 2 are calculated according to Eqs. (7)–(10). Some of them indeed are very small. The reasons for this include two aspects. First, the particles at these energies of the source term

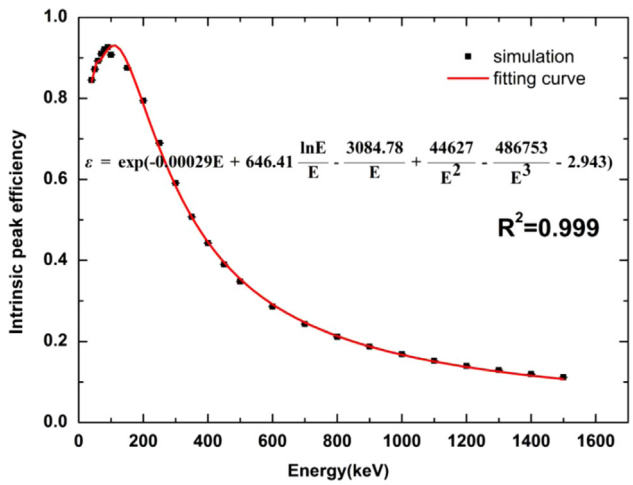

Fig. 6. Intrinsic peak efficiency calibration fitting curve of the $LaBr_3$ detector.

were very small so that the contributions to the spectrum also were very small. Secondly, the detection efficiencies of the $LaBr_3$ detector at higher energies are very low. Meanwhile, the used spectra in this study were the simulating spectra not the broadening spectra. Most of full-energy peaks could be separated from the scattered background in the spectra, so the total peak area method could be used here.

The relationship between the spectrum correction coefficient and the corresponding energy could be fitted to a curve according to the data in Table 2. Meanwhile, the statistical errors about the results obtained through MCNP simulation were less than 5% in the process of simulation.

As shown in Fig. 7, a good linear relationship could be found between the spectrum correction coefficient and the corresponding energy after the Fukushima nuclear accident. However, there was a sizable deviation from linearity at low energies. The cause on the deviation mainly includes two aspects. There is a big statistical fluctuation at low energies. Besides, the high-energy part has effect on the low-energy part owing to the scattering. The corresponding equation for the spectrum correction curve was fitted as follows:

$$R = 0.49741 + 0.00123E \quad (11)$$

where R was the spectrum correction coefficient, and E was the energy of the γ-ray (keV).

According to Eq. (11), when the energy was set to 80.9971 keV, the corresponding spectrum correction coefficient was 0.597. Then the real radioactivity of the radionuclide ^{133}Xe could be calculated using the correction coefficient and the net peak area of ^{133}Xe in the $LaBr_3$ detector.

Table 2
Spectrum correction coefficients of corresponding energies after the Fukushima nuclear accident.

Energy (keV)	Ideal peak area (A_i)	Ideal relative (R_{Ai})	Real peak area (B_i)	Real relative (R_{Bi})	Spectrum correction coefficient (R_i)
284	8.79E+02	7.51E−02	7.59E+01	6.18E−02	8.22E−01
364.5	1.17E+04	1.00E+00	1.23E+03	1.00E+00	1.00E+00
473	1.48E+02	1.26E−02	1.67E+01	1.36E−02	1.08E+00
569	2.48E+02	2.12E−02	3.13E+01	2.55E−02	1.20E+00
604	1.57E+03	1.34E−01	2.15E+02	1.74E−01	1.30E+00
661.7	1.14E+03	9.74E−02	1.49E+02	1.21E−01	1.24E+00
722.9	2.54E+02	2.17E−02	3.81E+01	3.10E−02	1.43E+00
795.8	1.38E+03	1.18E−01	2.04E+02	1.66E−01	1.41E+00
812.8	6.16E+00	5.26E−04	8.90E−01	7.24E−04	1.38E+00
852.2	2.34E+00	2.00E−04	4.02E−01	3.27E−04	1.63E+00
1260.4	1.63E+01	1.39E−03	3.75E+00	3.05E−03	2.19E+00
1365.2	4.86E+01	4.15E−03	1.14E+01	9.24E−03	2.23E+00
1457.5	4.92E+00	4.21E−04	1.22E+00	9.91E−04	2.35E+00
1678	5.43E+00	4.64E−04	1.51E+00	1.23E−03	2.65E+00
1791	4.38E+00	3.74E−04	1.16E+00	9.41E−04	2.52E+00

3.4. Spectrum correction results

According to Eqs. (9) and (10), the spectrum correction coefficient and the corresponding revised ideal value could be obtained. Then the deviation relative to the actual source term was calculated by comparing it with the information obtained by the HPGe detector. The corresponding data obtained through the meaning of the relative deviation are shown in Fig. 8.

As shown in Fig. 8, the deviation values relative to the actual source with correction was distinctly lower than those relative to the actual source without correction. The deviation values around the peak areas relative to the actual source after correction were less than 10%. Therefore, the spectrum correction method was feasible. Meanwhile, the maximum deviation value reduced from 1.65 to 0.035. It must be noted that the deviation values in Fig. 8 referred to the deviation values relative to the actual source about the ratio values of particles between other energies and 364.5 keV before and after the correction. And it did not refer to the relative deviation about the activity.

On the other hand, the spectrum correction factor at 80.9971 keV was 0.597 according to Eq. (11). Then the ratio of 80.9971 keV relative to 364.5 keV in the spectrum of the HPGe detector could be calculated using Eq. (10). Finally, the particle numbers of 80.9971 keV could be obtained according to the peak area of 364.5 keV in the spectrum of the HPGe detector. The deviation value relative to the actual activity of the radionuclide ^{133}Xe was 0.13 (the corrected activity of ^{133}Xe was 3.73×10^5 and the actual activity of ^{133}Xe was 3.28×10^5) with the correction. The deviation value was 5.68 without the correction. Apparently, the activity of the radionuclide 133Xe was more close to the actual value after the correction. In other words, the spectrum correction method was feasible.

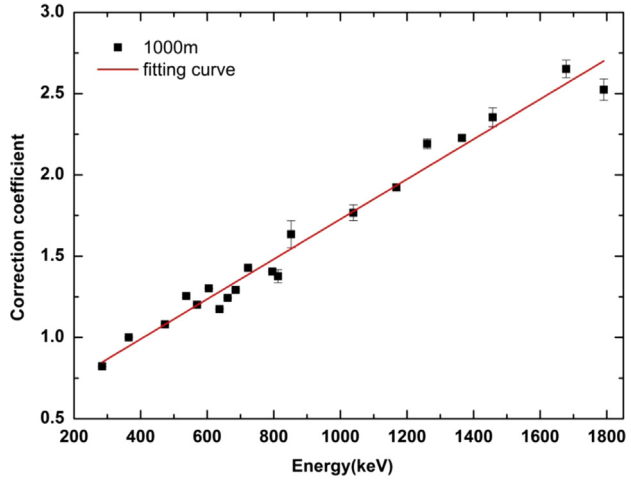

Fig. 7. Relationship between the spectrum correction coefficient and the corresponding energy.

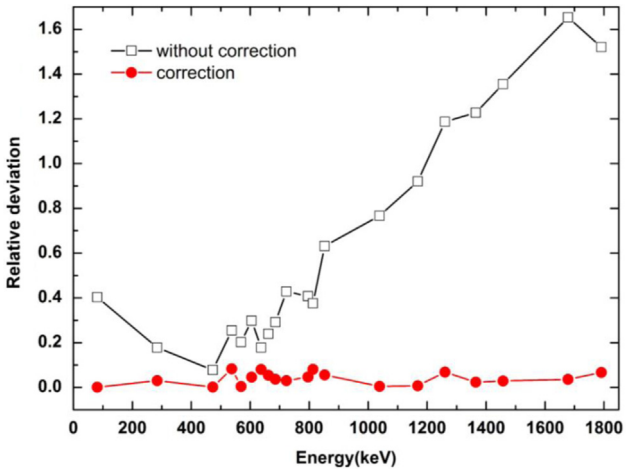

Fig. 8. Deviation values relative to the actual source with (full circles) and without correction (open squares).

3.5. Different sizes of the source term

The border of the radioactive plume is indefinite in actual conditions. Sizes of the source term mainly affect the particles entering the inside of the $LaBr_3$ detector. Specifically, the particle numbers increases with the increase of the size within a certain scale. And the scale is determined by the highest energy in the source term. The numbers remains to the same when the size is higher than the scale. Therefore, the popularity of the spectrum correction method in different sizes of the source term should be investigated. In this study, differences and relations among various sizes were mainly determined by changing the radius of the sphere volumetric source.

The radii of the sphere volumetric source were set to 1, 1.1 and 1.2 km. The detection spectra of the $LaBr_3$ detector were simulated using MC software. Then, the spectrum correction curves were calculated according to Eqs. (8)–(10). Moreover, in the process of simulation, the statistical errors about the results obtained through MCNP simulation were less than 5%.

The detection spectra of the $LaBr_3$ detector coincided with one another when the radii of the sphere volumetric source were 1, 1.1, and 1.2 km (Fig. 9(a) and (b)). As shown in Fig. 9(c), the spectrum correction curves could be approximately fitted using the same equation. Similarly, there was a sizable deviation from linearity at low energies because there is a big statistical fluctuation at low energies. Besides, the high-energy part has effect on the low-energy part owing to the scattering. When the radius of the sphere volumetric source increased to 1 km, the detection spectrum and the spectrum correction curve tended to coincide as the radius of the sphere volumetric source further increases.

Although the spectrum correction method was the same for a sphere volumetric source, the spectrum correction method must be applied to a sphere volumetric source with a radius smaller than 1 km.

The radii of the sphere volumetric source were set to 300, 500, 700, 900 and 1000 m. The detection spectra of the $LaBr_3$ detector were simulated using MCNP. Then, the spectrum correction curves were calculated according to Eqs. (8)–(10). Meanwhile, in the process of simulation, the statistical errors about the results obtained through MCNP simulation were less than 5%.

As shown in Fig. 10(a) and (b), the detection spectra of the $LaBr_3$ detector were gradually rising as the radius of the sphere volumetric source increases between 300 m and 1000 m. As shown in Fig. 10(c), good linear relationships could be found between the spectrum correction coefficient and the corresponding energy. There was a sizable deviation from linearity at low energies because there is a big statistical fluctuation at low energies. Besides, the high-energy part has effect on the low-energy part owing to the scattering. According to Fig. 10(c), the spectrum correction curves exhibited a rising trend as the increase of the radius of the sphere volumetric source increases between 300 m and 1000 m.

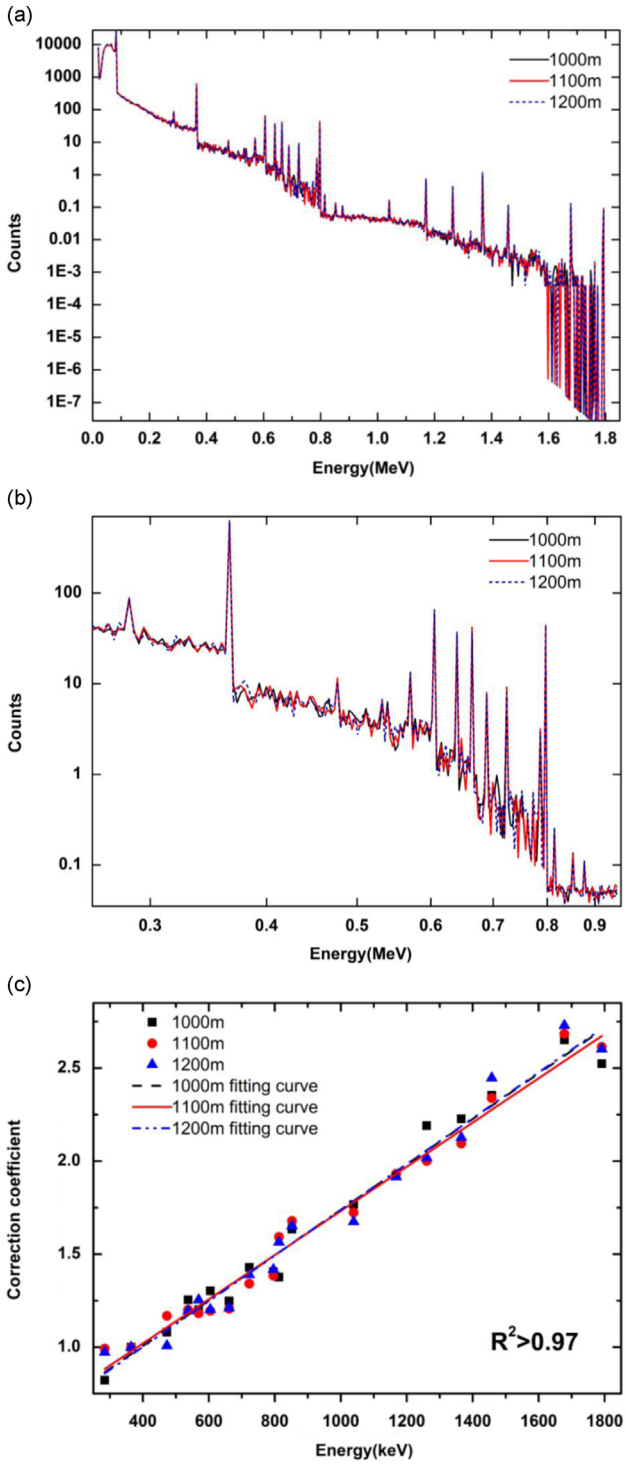

Fig. 9. Energy spectrums (a, b) and spectrum correction curves (c) of different sizes of the source term. (a) Whole energy spectrums, and (b) enlarged energy spectrums on (a) between 0.25 MeV and 9.2 MeV. The black solid, red solid, and blue dash curves are energy spectrums of 1 km, 1.1 km, and 1.2 km in (a) and (b). (For interpretation of the references to color in this figure legend, the reader is referred to the web version of this article.)

4. Conclusion

This study proposed a spectrum correction method for NH-UAV. The detection spectra of the $LaBr_3$ detector could be corrected according to the detection spectra of the HPGe detector. Then, the function of the fixed-point measurement in the corresponding category and activity of the radioactive nuclides within a small area could be realized. The detection spectra of the double detectors in NH-UAV were obtained using the Monte Carlo technique after the Fukushima nuclear accident. And the energies considered in this study was ranging from 80 keV to 1800 keV owing to the numbers of gamma rays emitted from radioactive materials after the Fukushima nuclear accident. The corresponding spectrum correction curves were calculated using ratio processing techniques about the net peak areas between the double detectors on the detection spectrum of the detection spectrum of the $LaBr_3$ detector according to the accuracy of the detection spectrum of the HPGe detector. A good linear relation existed between the spectrum correction coefficient and the corresponding energy

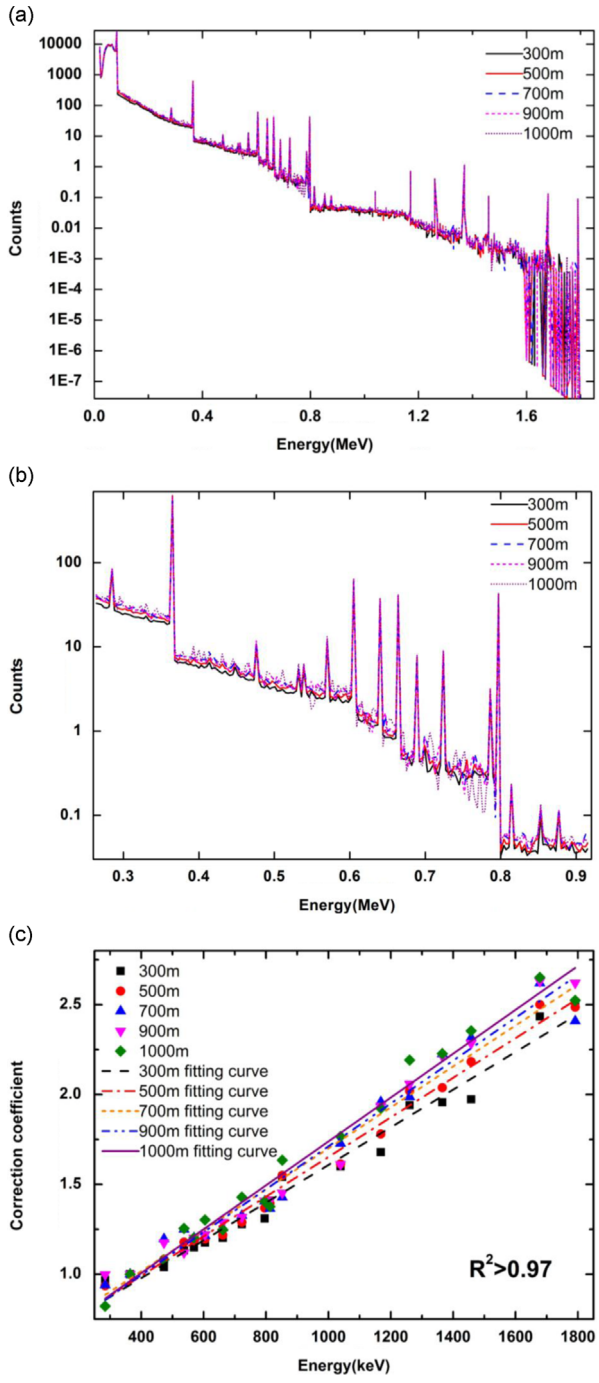

Fig. 10. Energy spectrums (a, b) and spectrum correction curves (c) of different sizes of the source term. (a) is whole energy spectrums, and (b) represents enlarged energy spectrums on (a) between 0.25 MeV and 9.2 MeV. The black solid, red solid, blue dash, magenta short dash and purple dot curves denote the energy spectrums of 300 m, 500 m, 700 m, 900 m and 1 km in (a) and (b). (For interpretation of the references to color in this figure legend, the reader is referred to the web version of this article.)

when the sphere volumetric source had a radius of 1 km. The spectrum correction method proposed in this study was verified to be feasible. Finally, different sizes of the source term were investigated. As the size of the source term increased gradually, the corresponding spectrum correction coefficients also increased. The spectrum correction coefficients remained the same when the radius of the sphere volumetric source increased to 1 km and the fitted spectrum correction curves also exhibited the same trend.

However, there were a number of limitations in this study. For example, the simulation conditions were too idealistic. We did not consider the influence of the radiation deposited on the ground in this study. Following the conclusion of the present paper, we plan to compare the differences and relations about the spectrum correction algorithm in different and more practical environments to obtain the data in a fixed place and in real time more accurately, such as in a largely non-uniform radiation cloud and considering the radiation from the ground. Meanwhile, we will take considerations about the detector resolution in the actual spectra in the next study.

Acknowledgments

The present work was supported by the Priority Academic Program Development of Jiangsu Higher Education Institutions and the National Defense Basic Scientific Research Project (Grant no. B2520133007).

References

[1] U. Korsbech, Danmarks Tekniske HoejskoleLyngby (Denmark). Afd. for Elektrofysik, 1993.
[2] K. Kurvinen, P. Smolander, R. Pöllänen, S. Kuukankorpi, M. Kettunen, J. Lyytinen, Journal of Environmental Radioactivity 81 (2005) 1.
[3] R. Pöllänen, H. Toivonen, K. Peräjärvi, T. Karhunen, T. Ilander, J. Lehtinen, K. Rintala, T. Katajainen, J. Niemelä, M. Juusela, Applied Radiation and Isotopes 67 (2009) 340.
[4] R. Pöllänen, H. Toivonen, K. Peräjärvi, T. Karhunen, P. Smolander, T. Ilander, K. Rintala, T. Katajainen, J. Niemelä, M. Juusela, Nova Biotechnologica et Chimica 2009 (2009) 129.
[5] Y. Sanada, A. Kondo, T. Sugita, Y. Nishizawa, Y. Yuuki, K. Ikeda, Y. Shoji, T. Torii, Exploration Geophysics 45 (2014) 3.
[6] H. Zafrir, A. Pernick, G. Steinitz, U. Yaffe, A. Grushka, Radiation Protection Dosimetry 50 (1993) 295.
[7] H. Arvela, M. Markkanen, H. Lemmelä, Radiation Protection Dosimetry 32 (1990) 177.
[8] ⟨http://www.wired.com/2008/03/robochoopers-to⟩.
[9] J. MacFarlane, O. Payton, A. Keatley, G. Scott, H. Pullin, R. Crane, M. Smilion, I. Popescu, V. Curlea, T. Scott, Journal of Environmental Radioactivity 136 (2014) 127.
[10] Y. Sanada, T. Torii, Journal of Environmental Radioactivity 139 (2015) 294.
[11] P.W. Eslinger, J.I. Friese, J.D. Lowrey, J.I. McIntyre, H.S. Miley, B.T. Schrom, Journal of Environmental Radioactivity 135 (2014) 94.
[12] H. Simgen, F. Arnold, H. Aufmhoff, R. Baumann, F. Kaether, S. Lindemann, L. Rauch, H. Schlager, C. Schlosser, U. Schumann, Journal of Environmental Radioactivity 132 (2014) 94.
[13] J.E. Sweezy, T.E. Booth, F.B. Brown, MCNP A General Monte Carlo N-Particle Transport Code, Version 5, Los Alamos National Laboratory, Los Alamos, 2003.
[14] ⟨http://japan.kantei.go.jp/kan/topics/201106/pdf/attach_04_2.pdf⟩.
[15] C. Gong, G. Zeng, L. Ge, X. Tang, C. Tan, Science China Technological Sciences 57 (2014) 1840.
[16] J. Boson, G. Ågren, L. Johansson, Nuclear Instruments and Methods in Physics Research A 587 (2008) 304.
[17] K. Abbas, F. Simonelli, F. D'Alberti, M. Forte, M. Stroosnijder, Applied Radiation and Isotopes 56 (2002) 703.
[18] G.A. Kumar, I. Mazumdar, D. Gothe, Nuclear Instruments and Methods in Physics Research A 609 (2009) 183.
[19] R. Casanovas, J. Morant, M. Salvadó, Nuclear Instruments and Methods in Physics Research A 675 (2012) 78.
[20] V. Peyres, E. García-Toraño, Nuclear Instruments and Methods in Physics Research A 580 (2007) 296.
[21] L. Loska, Applied Radiation and Isotopes 39 (1988) 475.
[22] H. Yücel, E. Köse, A. Esen, D. Bor, Applied Radiation and Isotopes 69 (2011) 890.